

# A Hierarchy of Topological and Superconducting States in Rhombohedral Hexalayer Graphene

Ron Q. Nguyen<sup>1,\*</sup>, Hai-Tian Wu<sup>1,\*</sup>, Erin Morissette<sup>1,\*</sup>, Naiyuan J. Zhang<sup>1,\*</sup>, Peiyu Qin<sup>1</sup>,  
K. Watanabe<sup>2</sup>, T. Taniguchi<sup>3</sup>, Aaron W. Hui<sup>1</sup>, D. E. Feldman<sup>1,5</sup>, and J.I.A. Li<sup>1,4†</sup>

<sup>1</sup>Department of Physics, Brown University, Providence, RI 02912, USA

<sup>2</sup>Research Center for Functional Materials, National Institute for Materials Science, 1-1 Namiki, Tsukuba 305-0044, Japan

<sup>3</sup>International Center for Materials Nanoarchitectonics,

National Institute for Materials Science, 1-1 Namiki, Tsukuba 305-0044, Japan

<sup>4</sup>Department of Physics, University of Texas at Austin, Austin, TX 78712, USA and

<sup>5</sup>Brown Theoretical Physics Center, Brown University, Providence, Rhode Island 02912, USA

(Dated: August 12, 2025)

**Superconductivity and the quantum Hall effect are conventionally viewed as mutually exclusive: the former is suppressed by magnetic fields, while the latter relies on them. Here, we report the surprising coexistence of these two phenomena in rhombohedral hexalayer graphene. In this system, a superconducting phase is not destroyed—but instead stabilized—by an out-of-plane magnetic field. Strikingly, this superconducting state coexists and competes with a sequence of quantum Hall states that appear at both integer and half-integer Landau level fillings. Both the superconducting and quantum Hall states exhibit sharply defined thermal transitions or crossovers, with nearly identical onset temperatures—pointing to a shared underlying mechanism. Taken together, our observations uncover an unprecedented interplay between superconducting and topological phases, challenging conventional paradigms and opening a new frontier in condensed matter physics.**

An enduring theme in the study of superconductivity is its fundamental antagonism with magnetic fields: superconducting phases are typically suppressed by even modest applied fields. It is therefore striking when superconductivity persists under large magnetic fields, defying conventional wisdom. Such behavior sets high- $T_c$  superconductors apart from their more mundane counterparts, establishing a vibrant research frontier over the last decades [1]. Even more exotic is the scenario in which a superconducting phase is not merely resilient to magnetic fields, but is in fact *stabilized* by them—pointing to an unconventional pairing symmetry. A prominent example is  $\text{UTe}_2$ , a candidate spin-triplet superconductor that exhibits field-induced reentrant superconductivity under strong magnetic fields [2–5].

When superconductivity persists to high magnetic fields, it opens the door to a rare and intriguing regime in which superconductivity coexists with another hallmark of two-dimensional (2D) electron systems: the quantum Hall effect. The interplay between these two phenomena has long been proposed as a key platform for realizing

fault-tolerant quantum computation, owing to the potential emergence of non-Abelian anyons and topological superconductivity [6–9]. Over the past decade, this coexistence has been explored extensively in engineered hybrid systems, where superconducting and quantum Hall regions are coupled across artificial interfaces [10–13], as well as in 2D material heterostructures hosting superconductivity and topological order at zero magnetic field [14, 15]. Despite these advances, achieving an intrinsic intertwinement of superconductivity and the quantum Hall effect within a single 2D electronic system—without relying on interface engineering—remains a central open challenge. A recent experimental report has identified such coexistence near zero magnetic field, sparking renewed interest in the possibility of anyonic superconductivity and its topological implications [16–19].

Here, we report an unprecedented form of interplay between superconductivity and topological order under a large out-of-plane magnetic field, realized in a rhombohedral hexalayer graphene (R6G) heterostructure [15, 20–23]. In stark contrast to all previously reported superconducting phases in 2D material heterostructures, the superconducting state in R6G is stabilized—rather than suppressed—by an external magnetic field. Strikingly, quantum Hall states emerge in direct proximity to this field-induced superconducting phase and form an unconventional sequence that includes both integer and half-integer Landau level (LL) fillings. Through multiple lines of experimental evidence, we identify a common microscopic origin underlying both phases. These findings place strong constraints on viable theoretical interpretations and point to a highly unconventional physical regime, where superconductivity and quantum Hall order emerge from a unified framework.

Facilitated by a dual-encapsulated heterostructure, as illustrated in Fig. 1a, the low-temperature phase space of R6G is governed by three independently tunable parameters: carrier density  $n$ , displacement field  $D$ , and out-of-plane magnetic field  $B_\perp$ . Superconductivity and the sequence of quantum Hall states are both confined within a unique boundary, which encircles a tilted cylindrical volume within this  $n$ - $D$ - $B$  space, as illustrated in

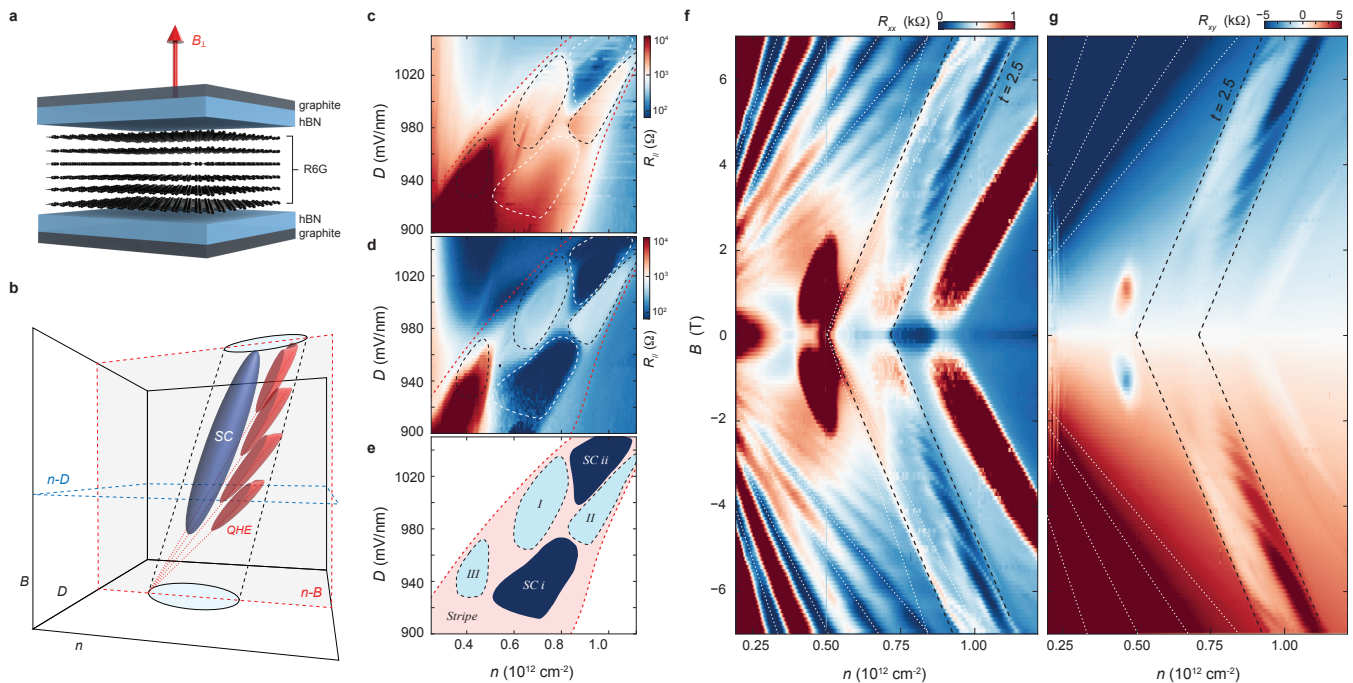


FIG. 1. **Multi-dimensional phase space of rhombohedral hexalayer graphene.** (a) Schematic of the R6G heterostructure. The red arrow indicates the out-of-plane magnetic field  $B_{\perp}$ . (b) Schematic phase diagram defined by carrier density  $n$ , displacement field  $D$ , and out-of-plane magnetic field  $B_{\perp}$ . (c, d)  $n$ - $D$  maps of longitudinal resistance measured at  $B = 0$ , with current flowing along the principal axes of (c) minimum and (d) maximum conductivity. (e) Annotated  $n$ - $D$  map highlighting prominent phases corresponding to panels (c, d). (f, g)  $n$ - $B$  maps measured at  $D = 967$  mV/nm, showing (f) longitudinal resistance  $R_{xx}$  and (g) transverse resistance  $R_{xy}$ . White dashed lines trace the trajectories of integer quantum Hall states, exhibiting integer Streda slopes. The boundaries of regime I, highlighted by the black dashed lines, follow a Streda slope of  $t = 2.5$ . In panel (f), white dotted lines show Streda slopes of 2 and 3, which clearly deviate from the boundaries of regime I.

Fig. 1b). For simplicity, we will refer to this portion of the phase space as regime I.

We begin by defining the boundary of regime I through its distinct transport signatures. To this end, we perform measurements across multiple two-dimensional slices of the  $n$ - $D$ - $B$  parameter space. In particular, we examine  $n$ - $D$  planes at five different values of out-of-plane magnetic field  $B_{\perp}$  (blue dashed lines in Fig. 1b), as well as  $n$ - $B$  planes at three fixed values of displacement field  $D$  (red dashed lines in Fig. 1b).

At zero magnetic field ( $B_{\perp} = 0$ ), the cross section of regime I is bounded by the electronic smectic phase and the striped superconducting state, both previously identified through angle-resolved transport studies [24]. The transport response across this regime is characterized in Figs. 1c-d, which show longitudinal resistance measured across the  $n$ - $D$  plane at  $B_{\perp} = 0$ , along two orthogonal principal axes corresponding to maximum and minimum conductivity. The smectic phase occupies the region of pronounced transport anisotropy (see Fig. M2b), highlighted by the red-shaded area in Fig. 1e. Within this anisotropic regime, two superconducting phases—denoted SC i and SC ii—emerge concurrently with the smectic order and inherit its strong directional character [24].

The  $B_{\perp} = 0$  cross-section of regime I appears as a metallic phase situated between SC i and SC ii, enclosed by black dashed lines in Figs. 1c-e. As  $B_{\perp}$  increases, the boundaries of regime I trace a well-defined trajectory in the  $n$ - $B$  plane, marked by peaks in the longitudinal resistance  $R_{xx}$  and abrupt jumps in the Hall resistance  $R_{xy}$ . These boundaries, indicated by black dashed lines in Fig. 1f-g, exhibit a Streda slope of  $t = 2.5$  [25–27].

Within the stripe regime, two additional metallic phases—regime II and regime III—are highlighted in Figs. 1c-e. These phases resemble regime I in their transport characteristics and exhibit well-defined boundaries in the  $n$ - $B$  plane, following distinct Streda slopes:  $t = 2$  for regime II and  $t = 3.5$  for regime III (see Fig. M8 for further discussion). The presence of such sharply delineated, evolving boundaries is intriguing. Although a well-defined Streda slope often signals a topological phase, we do not observe transport features typically associated with incompressible quantum Hall states [28]. We revisit this issue later in the context of additional experimental evidence.

In addition to their distinct Streda slopes, regimes I, II, and III exhibit significantly reduced transport anisotropy compared to the surrounding stripe phase (see Fig. M2c and Fig. M3a), suggesting the emergence of a competing

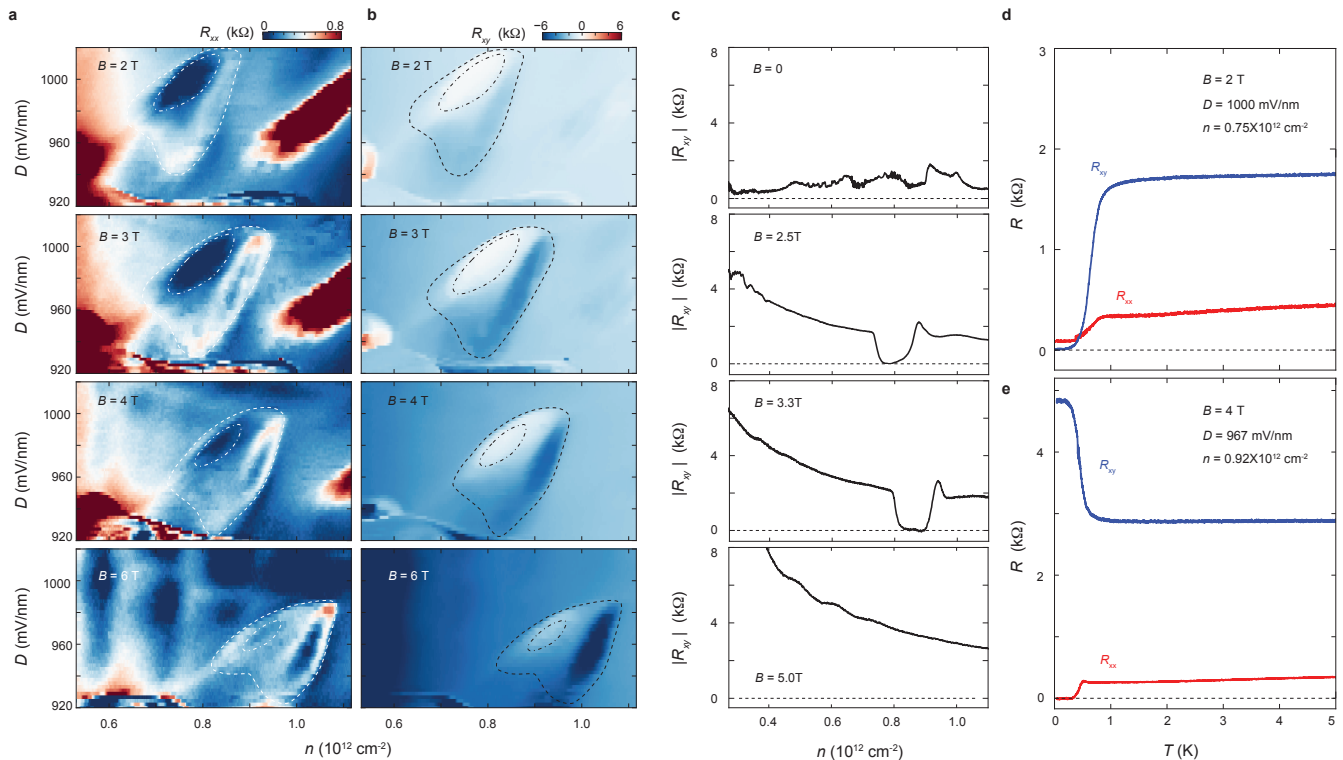


FIG. 2.  $B_{\perp}$ -stabilized superconductivity and coexisting quantum Hall state.  $n$ - $D$  maps of (a)  $R_{xx}$  and (b)  $R_{xy}$  measured at different values of  $B_{\perp}$ . The dashed line outlines the boundary of regime I, while the dash-dotted line encloses the superconducting phase. (c) Line cuts of  $|R_{xy}|$  as a function of  $n$  at  $D = 1000$  mV/nm, measured at various values of  $B_{\perp}$ . (d, e) Temperature dependence of  $R_{xx}$  (red) and  $R_{xy}$  (blue) measured from (d) the  $B_{\perp}$ -stabilized superconducting phase and (e) the adjacent quantum Hall state.

order that disrupts the underlying smectic state.

Figures 2a–b show  $n$ - $D$  maps of the longitudinal and Hall resistances measured at various values of  $B_{\perp}$ . At each field, regime I is delineated by peaks in  $R_{xx}$ , defining a boundary that shifts systematically with  $B_{\perp}$  in both carrier density  $n$  and displacement field  $D$ . These evolving boundaries are marked by dashed lines in Figs. 2a–b. Most notably, upon applying a non-zero  $B_{\perp}$ , a superconducting pocket emerges on the low-density side of regime I, while a sequence of quantum Hall states appears on the high-density side.

The superconducting phase—enclosed by dash-dotted lines—is identified by vanishing longitudinal resistance  $R_{xx}$  and zero Hall resistance  $R_{xy}$ , appearing as dark blue and white, respectively, in the color maps. Figure 2c presents line cuts of the transport response as a function of  $n$ , taken at fixed  $D = 1000$  mV/nm and varying  $B_{\perp}$ . At  $B_{\perp} = 0$ , the system remains resistive across the entire density range. In contrast, at  $B_{\perp} = 2.5$  and 3.3 T, a superconducting dome is clearly visible, characterized by a sharp drop to zero resistance. Upon further increasing  $B_{\perp}$  to 5 T, the superconducting phase is fully suppressed.

On the high-density side of the superconducting region, we observe the emergence of a distinct phase along the upper boundary of regime I, exhibiting transport sig-

natures that sharply contrast with those of the superconducting state. In this regime, vanishing  $R_{xx}$  is accompanied by a pronounced peak in  $R_{xy}$ . The corresponding conductivity matrix is characterized by vanishing diagonal (longitudinal) components and finite, antisymmetric off-diagonal (Hall) components. In Fig. 3, we show that this high-density state evolves with varying  $B_{\perp}$  along a well-defined Streda slope—a hallmark of an incompressible quantum Hall state. Notably, the minima in  $R_{xx}$  for each quantum Hall state are flanked by resistive peaks, suggesting that these states arise from strong electronic interactions.

Remarkably, both the superconducting and quantum Hall phases exhibit sharply defined onsets as a function of temperature (Fig. 2d–e). The  $R$ - $T$  curves in Fig. 2d display behavior consistent with a superconducting transition, characterized by a critical temperature  $T_c \approx 0.5$  K. In contrast, the similarly sharp onset observed for the quantum Hall state in Fig. 2e is highly unusual. Conventional quantum Hall states typically display a gradual thermal activation in  $R_{xx}$ , while  $R_{xy}$  remains largely quantized and temperature-independent (see Fig. M6). The abrupt temperature dependence observed here suggests an unconventional origin for the quantum Hall state, a possibility we return to in light of additional

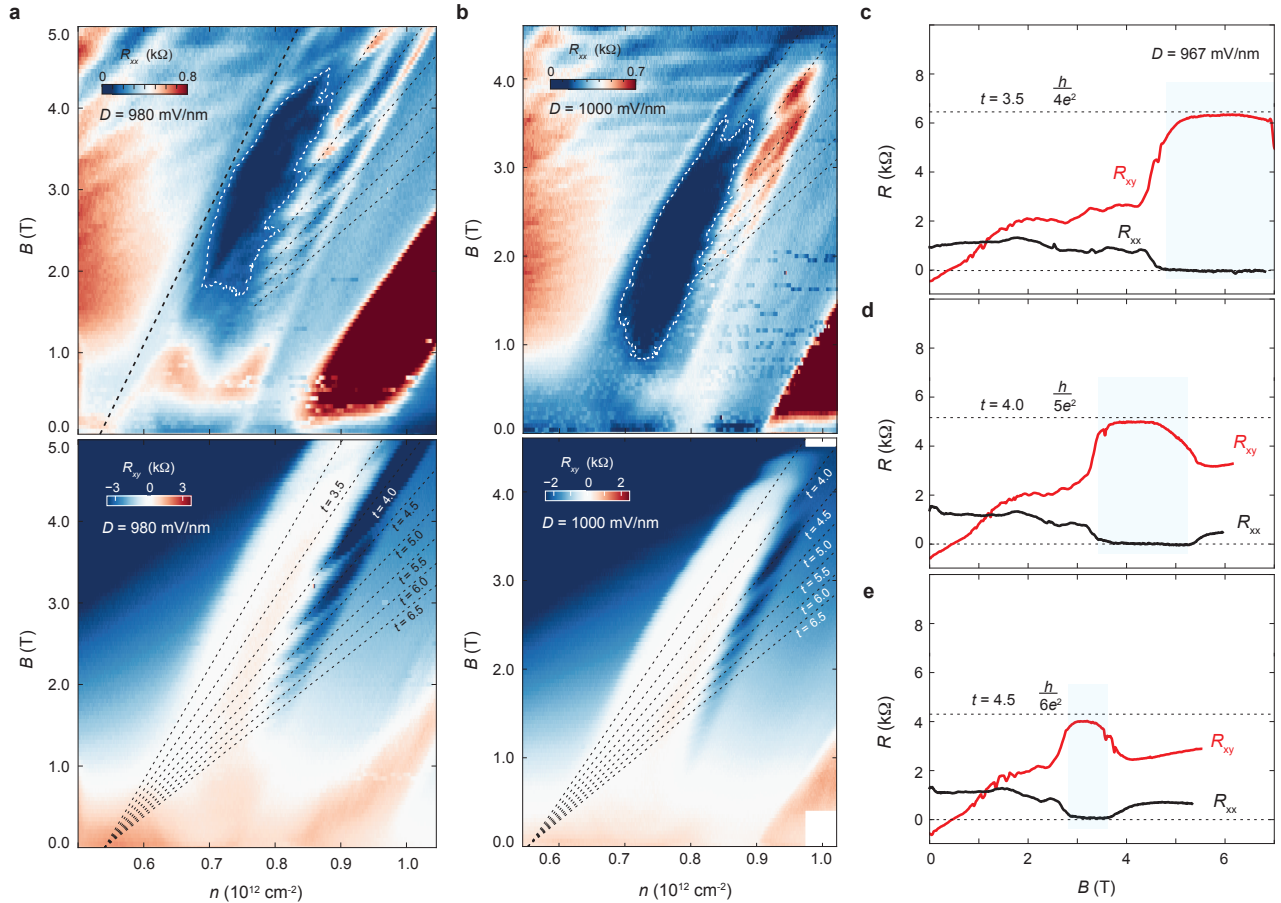


FIG. 3. **An exotic sequence of quantum Hall states.** (a, b)  $n$ - $B$  map of  $R_{xx}$  (top panel) and  $R_{xy}$  (bottom panel) measured at (a)  $D = 980$  mV/nm and (b)  $D = 1000$  mV/nm. The superconducting region is enclosed by a white dashed line in the top panel, while the sequence of quantum Hall states forms a Landau fan, marked by black dashed lines.

experimental evidence discussed below.

Next, we investigate the unusual robustness of the superconducting phase against  $B_{\perp}$  in Figs. 3a–b, which present transport measurements across  $n$ - $B$  planes intersecting regime I at fixed displacement fields. A pronounced resistive peak in  $R_{xx}$  appears within regime I around  $B_{\perp} = 1$  T, marking the lower-field boundary for both the superconducting and quantum Hall states. We interpret this feature as indicative of a transition in the underlying electronic order.

Given that the superconducting phase is stabilized above this resistive feature, it is natural to consider a transition in the underlying isospin order. For  $B_{\perp} > 1$  T, regime I is expected to be fully polarized in both spin and valley degrees of freedom. In this high-field regime, superconductivity likely originates from Cooper pairing in an odd orbital angular momentum channel, consistent with a  $p$ -wave pairing symmetry [29]. At lower fields ( $B_{\perp} < 1$  T), the ground state may be only partially polarized. Fermiology analysis reveals that regime I lies between a half-metallic phase at low density and a quarter-metallic phase at high density, consistent with partial

isospin polarization in the intermediate regime. However, this interpretation may be at odds with the chiral nature of the SC i and SC ii phases observed near zero field [23], which have been argued to emerge from a fully isospin-polarized normal state.

An alternative interpretation is that the resistive feature marks a  $B_{\perp}$ -driven reconstruction of momentum-space order. In rhombohedral graphene (R6G), rotational symmetry breaking has been attributed to spontaneous polarization in momentum space [24, 30–33]. The stability of the superconducting phase may therefore depend sensitively on the momentum-space configuration of the Fermi surface, particularly within a quarter-metallic state [34, 35]. This possibility is further supported by the observed  $B_{\perp}$ -dependent rotation of the principal axis within regime I (see Fig. M3).

On the high-density side of regime I, quantum Hall states emerge along well-defined linear trajectories in the  $n$ - $B$  plane, tracing minima in  $R_{xx}$  and maxima in  $|R_{xy}|$ . These trajectories, marked by black dashed lines in Fig. 3a–b, form a characteristic pattern reminiscent of a Landau fan diagram [36]. However, the sequence of

quantum Hall states in this regime exhibits several unusual features that set it apart from conventional Landau fans.

In particular, the observed trajectories follow Streda slopes corresponding to both integer and half-integer Landau level (LL) fillings, with  $\nu = N/2$ , where  $N \in \mathbb{Z}$ . This pattern would conventionally imply the emergence of incompressible states at fully and half-filled LLs. However, a striking discrepancy arises between the inferred filling factors and the actual Hall quantization. As shown in Fig. 3c–e, line cuts along representative trajectories reveal vanishing  $R_{xx}$ , signaling fully developed incompressible states, while the Hall resistance  $R_{xy}$  remains quantized at *integer* multiples of the conductance quantum.

This mismatch between the Streda slope and Hall quantization suggests an unconventional origin. One possibility is a reduction in the effective LL degeneracy by a factor of two, such that a sequence of integer quantum Hall states occurs along Streda slope at  $\nu = N/2$ .

In addition, the observed quantum Hall states exhibit a highly unusual hierarchical structure. In conventional two-dimensional electron systems, incompressible states at half-filled Landau levels—commonly associated with even-denominator fractional quantum Hall effects (FQHE)—possess significantly smaller energy gaps than their integer counterparts and exhibit strong dependence on the out-of-plane magnetic field  $B_{\perp}$ . By contrast, quantum Hall states in regime I display comparable robustness between integer and half-integer Streda slopes, evidenced by nearly identical onset temperature, as illustrated in Fig. 4a. This offers further indication that the underlying incompressible states are IQHE in nature.

Moreover, the onset temperature of quantum Hall states remain nearly constant across a wide range of  $B_{\perp}$ . This temperature dependence closely mirrors that of the superconducting phase. As shown in Fig. 4b, the superconducting transition remains essentially unchanged across a broad range of  $B_{\perp}$ , and its transition temperature closely matches the onset temperature of the adjacent quantum Hall states.

A close correlation between the quantum Hall and superconducting states is further illustrated in Fig. 4c–d. An  $n$ – $T$  map of the transport response, taken at fixed  $B_{\perp}$  and displacement field  $D$ , reveals that the superconducting transition and the onset of the quantum Hall effect trace a continuous envelope that evolves smoothly with carrier density  $n$ . A similar correspondence is observed in the current–voltage (I–V) characteristics, as shown in Fig. 4d. The quantum Hall state, which appears on the high-density side of regime I, exhibits pronounced nonlinearity in its transport response, evidenced by large variations in the differential resistance  $dV/dI$  in both longitudinal and transverse channels. This nonlinearity defines a sharp threshold in the d.c. current bias, which closely aligns with the critical current of the su-

perconducting state—marked by a peak in  $dV/dI$ . Taken together, these coordinated behaviors strongly suggest a shared origin underlying both the superconducting and quantum Hall states.

In the following, we discuss potential mechanisms that may underlie the intriguing coexistence of superconductivity and quantum Hall states. Any viable explanation must account for the following key experimental observations. First, a superconducting phase is stabilized—rather than suppressed—by an out-of-plane magnetic field  $B_{\perp}$ . That the superconducting phase persists beyond  $B_{\perp} > 4$  T is unprecedented in two-dimensional superconductors. Second, the sequence of quantum Hall states emerges at both integer and half-integer filling factors, displaying a prominent mismatch between the Streda slope and Hall quantization. Third, the unique interplay between the superconducting and quantum Hall phases—including their shared onset temperature and adjacent locations in phase space—suggests a common underlying mechanism.

We consider a scenario involving charge density wave (CDW) order, wherein electrons are localized to form an array of insulating islands, schematically illustrated as white circles in Fig. 4e–g. In this picture, the extent of regime I is governed by the stability of the CDW order across the  $n$ – $D$ – $B$  phase space. As the carrier density  $n$  increases from the low-density boundary of regime I, itinerant electrons are introduced occupying the regions between the insulating islands. These itinerant electrons contribute to conductive transport at  $B_{\perp} = 0$  and enable the emergence of superconductivity and quantum Hall states at  $B_{\perp} > 1$  T. The boundary of the CDW phase traces a finite Streda slope in the  $n$ – $B$  plane, suggesting that the reconstructed electronic bands feature non-zero Berry curvature. However, due to the mismatch between Streda slope and Hall plateau, the exact Streda slope likely is not representing the actual Berry curvature.

In the presence of an out-of-plane magnetic field, LL formation of the itinerant electrons gives rise to the sequence of quantum Hall states observed in regime I (Fig. 4f). Within this framework, these quantum Hall states resemble a re-entrant integer quantum Hall effect [37–39]. Because electrons localized within the insulating islands do not contribute to transport, the effective carrier density is reduced. This reduction yields Hall plateaus comparable to those of the IQHE emanating from the CNP, indicating the same effective density occurring at distinct values of the actual carrier density (Fig. 2b and Fig. 3a–b).

Crucially, the emergence of CDW order decouples the Streda slope from the quantized Hall plateau. When extra charge carriers are added to the sample, they preferentially occupy the regions between insulating islands. As a result, the effective density of itinerant electrons,  $n^*$ , increases at a faster rate compared to the actual electron density  $n$ . This naturally accounts for the mismatch be-

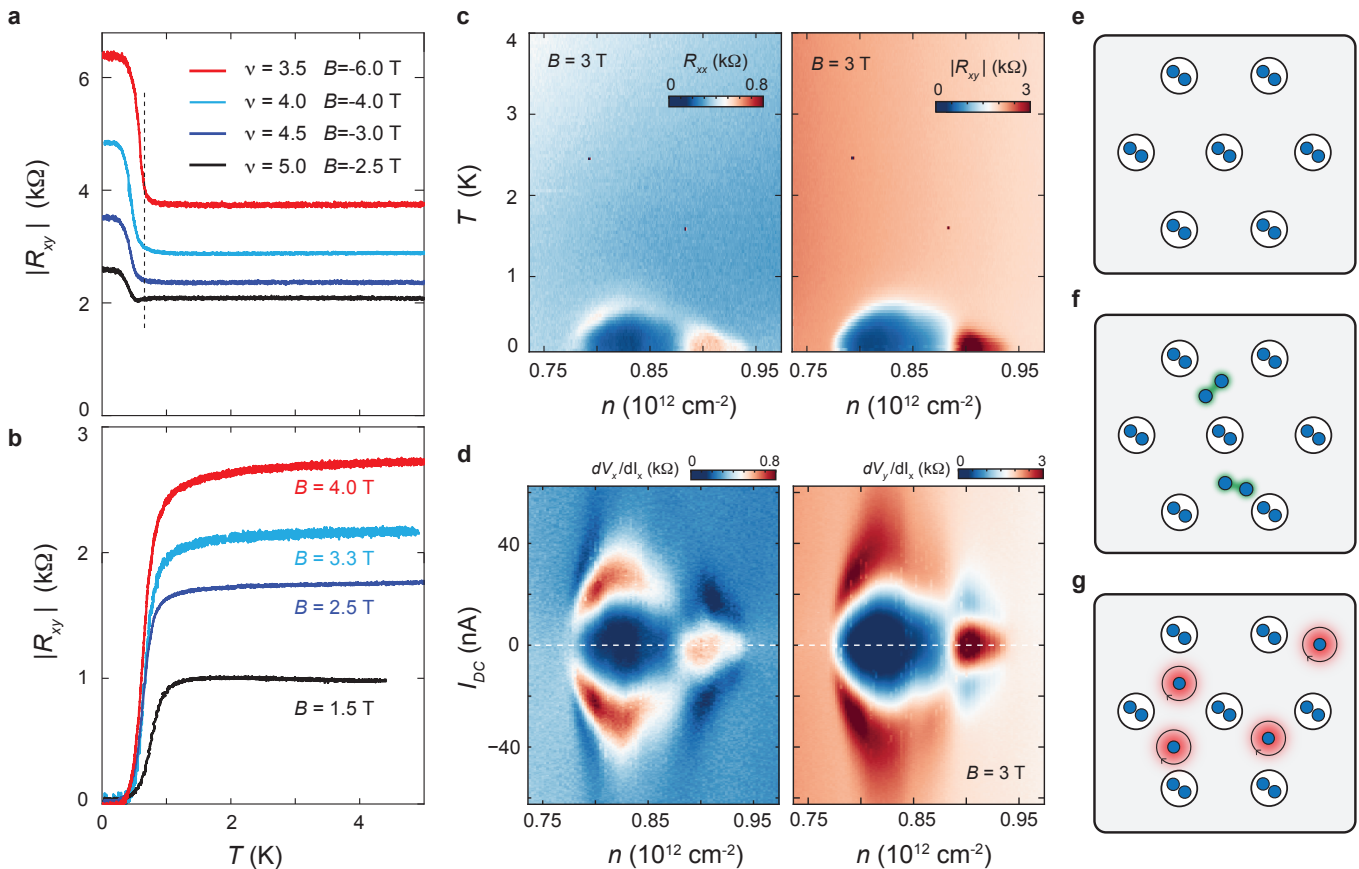


FIG. 4. **Transition temperature and critical current.** (a, b) Temperature dependence of  $R_{xy}$  measured at different  $B_{\perp}$  values within (a) quantum Hall states and (b) the superconducting phase. (c) Longitudinal resistance  $R_{xx}$  (left panel) and transverse resistance  $R_{xy}$  (right panel) as functions of carrier density  $n$  and temperature  $T$  across the superconducting and quantum Hall states at  $B_{\perp} = 3$  T and  $D = 1000$  mV/nm. (d) Differential resistance  $dV/dI$  as a function of  $n$  and d.c. current bias  $I_{DC}$  at  $B_{\perp} = 3$  T and  $D = 1000$  mV/nm. Data in the left (right) panel were obtained in the longitudinal (transverse) measurement configuration. (e–g) Schematic diagrams illustrating possible mechanisms underlying superconductivity and quantum Hall states. (e) Regime I is associated with the emergence of a CDW order, with insulating islands shown as white circles. (f, g) Away from the low-density boundary of regime I, itinerant electrons occupy the regions between insulating islands, giving rise to (f) superconductivity on the low-density side of regime I and (g) the quantum Hall effect on the high-density side of regime I.

tween the Streda slope and the quantized Hall plateau.

This framework leads to an intriguing scenario in which superconductivity coexists with charge density wave (CDW) order, occupying the regions between insulating CDW islands (Fig. 4g). These metallic regions supports superconducting transport at low temperatures. The close proximity of the superconducting and quantum Hall phases in the phase diagram—and their nearly identical onset temperatures—suggests that both originate from the same population of itinerant electrons, with superconductivity (quantum Hall states) stabilized in the low-density (high-density) limit. As the temperature increases, the CDW order melts, disrupting the spatial segregation between localized and itinerant carriers. This melting transition naturally accounts for the sharply defined thermal onset observed in both superconducting and quantum Hall responses (Fig. 4a–b).

Besides the CDW scenario, we note that alternative explanations may still be viable. Nonetheless, the discovery of a superconducting phase that is stabilized—rather than suppressed—by an out-of-plane magnetic field, and its striking connection to an exotic sequence of quantum Hall states, represents a fundamentally new phenomenon. The intriguing interplay between superconductivity and quantum Hall effect presents a compelling challenge to existing theoretical paradigms, which is expected to stimulate broad future interest into emergent phenomena of strongly interacting electrons in 2D material heterostructures.

## ACKNOWLEDGMENTS

This material is based on the work supported by the Air Force Office of Scientific Research under award no. FA9550-23-1-0482. R.Q.N., N.J.Z, and J.I.A.L. acknowledge support from the Air Force Office of Scientific Research. E.M. acknowledge support from U.S. National Science Foundation under Award DMR-2143384. K.W. and T.T. acknowledge support from the JSPS KAKENHI (Grant Numbers 21H05233 and 23H02052) and World Premier International Research Center Initiative (WPI), MEXT, Japan. Part of this work was enabled by the use of pyscan ([github.com/sandialabs/pyscan](https://github.com/sandialabs/pyscan)), scientific measurement software made available by the Center for Integrated Nanotechnologies, an Office of Science User Facility operated for the U.S. Department of Energy. D.E.F. was supported in part by the National Science Foundation under grant No. DMR-2204635.

\* These authors contributed equally to this work.

† [jia.li@austin.utexas.edu](mailto:jia.li@austin.utexas.edu)

- [1] P. W. Phillips, E. La Nave, and E. Huang, “High-temperature superconductivity,” *Nature Reviews Physics* **3**, 454–473 (2021).
- [2] Sheng Ran, I-Lin Liu, Yun Suk Eo, Daniel J. Campbell, Paul M. Neves, Wesley T. Fuhrman, Shanta R. Saha, Christopher Eckberg, Hyunsoo Kim, David Graf, Fedor Balakirev, John Singleton, Johnpierre Paglione, and Nicholas P. Butch, “Extreme magnetic field-boosted superconductivity,” *Nature Physics* **15**, 1250–1254 (2019).
- [3] Sheng N. Ran, Christopher Eckberg, Qing-Ping Ding, Yuji Furukawa, Tristin Metz, Shanta R. Saha, I-Lin Liu, Mark Zic, Hyunsoo Kim, Johnpierre Paglione, and Nicholas P. Butch, “Nearly ferromagnetic spin-triplet superconductivity,” *Science* **365**, 684–687 (2019).
- [4] Dai Aoki, Georg Knebel, Kenji Ishida, Aurélien Pourret, Daniel Braithwaite, Gérard Lapertot, Qun Niu, Marek Valiska, Hisatomo Harima, and Jacques Flouquet, “Unconventional superconductivity in heavy fermion  $UTe_2$ ,” *Journal of the Physical Society of Japan* **88**, 043702 (2019).
- [5] S. K. Lewin, C. E. Frank, S. Ran, J. P. Paglione, and N. P. Butch, “A review of  $UTe_2$  at high magnetic fields,” *Reports on Progress in Physics* **86** (2023), 10.1088/1361-6633/acfb93.
- [6] Chetan Nayak, Steven H. Simon, Ady Stern, Michael Freedman, and Sankar Das Sarma, “Non-Abelian anyons and topological quantum computation,” *Reviews of Modern Physics* **80**, 1083–1159 (2008).
- [7] Sankar Das Sarma, Michael Freedman, and Chetan Nayak, “Majorana zero modes and topological quantum computation,” *npj Quantum Information* **1** (2015).
- [8] Lucila Peralta Gavensky, Gonzalo Usaj, and C. Alejandro Balseiro, “Majorana fermions on the quantum Hall edge,” *Physical Review Research* **2**, 033218 (2020).
- [9] Jason Alicea and Paul Fendley, “Topological phases with parafermions: Theory and blueprints,” *Annual Review of Condensed Matter Physics* **7**, 119–139 (2016).
- [10] F. Amet, C. T. Ke, I. V. Borzenets, J. Wang, K. Watanabe, T. Taniguchi, R. S. Deacon, M. Yamamoto, Y. Bomze, S. Tarucha, and G. Finkelstein, “Supercurrent in the quantum Hall regime,” *Science* **352**, 966–969 (2016).
- [11] Gil-Ho Lee, Kuan-Feng Huang, Dmitri K. Efetov, Di S. Wei, Sean Hart, Takashi Taniguchi, Kenji Watanabe, Amir Yacoby, and Philip Kim, “Inducing superconducting correlation in quantum Hall edge states,” *Nature Physics* **13**, 693–698 (2017).
- [12] Önder Gül, Yuval Ronen, Seung Hwan Lee, Hassan Shapourian, Jonathan Zauberman, Young Hyun Lee, Kenji Watanabe, Takashi Taniguchi, Ashvin Vishwanath, Amir Yacoby, and Philip Kim, “Andreev reflection in the fractional quantum Hall state,” *Physical Review X* **12**, 021057 (2022).
- [13] Lingfei Zhao, Zubair Iftikhar, Trevyn F. Q. Larson, Ethan G. Arnault, Kenji Watanabe, Takashi Taniguchi, Fran çois Amet, and Gleb Finkelstein, “Loss and decoherence at the quantum Hall-superconductor interface,” *Phys. Rev. Lett.* **131**, 176604 (2023).
- [14] Petr Stepanov, Ming Xie, Takashi Taniguchi, Kenji Watanabe, Xiaobo Lu, Allan H MacDonald, B Andrei Bernevig, and Dmitri K Efetov, “Competing zero-field Chern insulators in superconducting twisted bilayer graphene,” arXiv preprint arXiv:2012.15126 (2020).
- [15] Youngjoon Choi, Ysun Choi, Marco Valentini, Caitlin L Patterson, Ludwig FW Holleis, Owen I Sheekey, Hari Stoyanov, Xiang Cheng, Takashi Taniguchi, Kenji Watanabe, *et al.*, “Superconductivity and quantized anomalous Hall effect in rhombohedral graphene,” *Nature*, 1–6 (2025).
- [16] Fan Xu, Zheng Sun, Jiayi Li, Ce Zheng, Cheng Xu, Jingjing Gao, Tongtong Jia, Kenji Watanabe, Takashi Taniguchi, Bingbing Tong, Li Lu, Jinfeng Jia, Zhiwen Shi, Shengwei Jiang, Yuanbo Zhang, Yang Zhang, Shiming Lei, Xiaoxue Liu, and Tingxin Li, “Signatures of unconventional superconductivity near reentrant and fractional quantum anomalous Hall insulators,” arXiv preprint arXiv:2504.06972 (2025), arXiv:2504.06972 [cond-mat.supr-con].
- [17] Pavel A. Nosov, Zhaoyu Han, and Eslam Khalaf, “Anyon superconductivity and plateau transitions in doped fractional quantum anomalous Hall insulators,” arXiv preprint arXiv:2506.02108 (2025).
- [18] Fabian Pichler, Clemens Kuhlenkamp, Michael Knap, and Ashvin Vishwanath, “Microscopic mechanism of anyon superconductivity emerging from fractional Chern insulators,” arXiv preprint arXiv:2506.08000 (2025).
- [19] Zhengyan Darius Shi and T. Senthil, “Doping a fractional quantum anomalous Hall insulator,” arXiv preprint arXiv:2409.20567 (2024), arXiv:2409.20567 [cond-mat.str-el].
- [20] Haoxin Zhou, Tian Xie, Areg Ghazaryan, Tobias Holder, James R Ehrets, Eric M Spanton, Takashi Taniguchi, Kenji Watanabe, Erez Berg, Maksym Serbyn, *et al.*, “Half-and quarter-metals in rhombohedral trilayer graphene,” *Nature* **598**, 429–433 (2021).
- [21] Haoxin Zhou, Tian Xie, Takashi Taniguchi, Kenji Watanabe, and Andrea F Young, “Superconductivity in rhombohedral trilayer graphene,” *Nature* **598**, 434–438 (2021).
- [22] Haoxin Zhou, Ludwig Holleis, Yu Saito, Liam Cohen, William Huynh, Caitlin L Patterson, Fangyuan Yang,

- Takashi Taniguchi, Kenji Watanabe, and Andrea F Young, “Isospin magnetism and spin-polarized superconductivity in Bernal bilayer graphene,” *Science* **375**, 774–778 (2022).
- [23] Xinyuan Han, Elliott Morissette, Cheng Zhang, Yin Lin, and Leo Yu Li, “Signatures of chiral superconductivity in rhombohedral graphene,” *Nature* **617**, 389–395 (2025).
- [24] Erin Morissette, Peiyu Qin, Hai-Tian Wu, Naiyuan J Zhang, K Watanabe, T Taniguchi, and JIA Li, “Superconductivity, anomalous Hall effect, and stripe order in rhombohedral hexalayer graphene,” arXiv preprint arXiv:2504.05129 (2025).
- [25] P. Středa and L. Smrčka, “Magneto-oscillatory effects in two-dimensional systems with spin-orbit interaction,” *Journal of Physics C: Solid State Physics* **16**, L895–L900 (1983).
- [26] A. Widom, “Thermodynamic Hall impedance for two-dimensional models,” *Phys. Rev. B* **28**, 4858–4859 (1983).
- [27] A. H. MacDonald and P. Středa, “Quantized Hall effect and edge currents,” *Phys. Rev. B* **29**, 1616–1619 (1984).
- [28] Yi Huang, Jian Zang, Fang Xu, and M. Zahid Hasan, “Apparent inconsistency between Streda formula and Hall conductivity in reentrant integer quantum anomalous hall effect in twisted MoTe<sub>2</sub>,” arXiv preprint arXiv:2506.10965 (2025).
- [29] P. W. Anderson and P. Morel, “Generalized Bardeen-Cooper-Schrieffer states and the proposed low-temperature phase of liquid He<sup>3</sup>,” *Physical Review* **123**, 1911–1934 (1961).
- [30] Erin Morissette, Peiyu Qin, K Watanabe, T Taniguchi, and JIA Li, “Intertwined nematicity, multiferroicity, and nonlinear Hall effect in rhombohedral pentalayer graphene,” arXiv preprint arXiv:2503.09954 (2025).
- [31] Zhiyu Dong, Margarita Davydova, Olumakinde Ogunnaike, and Leonid Levitov, “Isospin- and momentum-polarized orders in bilayer graphene,” *Phys. Rev. B* **107**, 075108 (2023).
- [32] Jeil Jung, Marco Polini, and Allan H MacDonald, “Persistent current states in bilayer graphene,” *Physical Review B* **91**, 155423 (2015).
- [33] Chunli Huang, Tobias MR Wolf, Wei Qin, Nemin Wei, Igor V Blinov, and Allan H MacDonald, “Spin and orbital metallic magnetism in rhombohedral trilayer graphene,” *Physical Review B* **107**, L121405 (2023).
- [34] Maximilian Geier, Marina Davydova, and Liang Fu, “Chiral and topological superconductivity in isospin-polarized multilayer graphene,” arXiv preprint arXiv:2409.12345 (2024), [arXiv:2409.12345](https://arxiv.org/abs/2409.12345) [[cond-mat.supr-con](https://arxiv.org/archive/cond-mat)].
- [35] Guillermo Parra-Martinez, Alejandro Jimeno-Pozo, Vo Tien Phong, Hector Sainz-Cruz, Daniel Kaplan, Peleg Emanuel, Yuval Oreg, Pierre A Pantaleon, Jose Angel Silva-Guillen, and Francisco Guinea, “Band renormalization, quarter metals, and chiral superconductivity in rhombohedral tetralayer graphene,” arXiv preprint arXiv:2502.19474 (2025).
- [36] Yuanbo Zhang, Yan-Wen Tan, Horst L Stormer, and Philip Kim, “Experimental observation of the quantum Hall effect and Berry’s phase in graphene,” *nature* **438**, 201 (2005).
- [37] J. P. Eisenstein, K. B. Cooper, L. N. Pfeiffer, and K. W. West, “Insulating and fractional quantum Hall states in the first excited Landau level,” *Phys. Rev. Lett.* **88**, 076801 (2002).
- [38] J. S. Xia, W. Pan, C. L. Vicente, E. D. Adams, N. S. Sullivan, H. L. Stormer, D. C. Tsui, L. N. Pfeiffer, K. W. Baldwin, and K. W. West, “Electron correlation in the second Landau level: A competition between many nearly degenerate quantum phases,” *Phys. Rev. Lett.* **93**, 176809 (2004).
- [39] Bertrand I Halperin and Jainendra K Jain, *Fractional quantum Hall effects: New developments* (World Scientific, 2020).
- [40] Naiyuan James Zhang, Jiang-Xiazi Lin, Dmitry V. Chichinadze, Yibang Wang, Kenji Watanabe, Takashi Taniguchi, Liang Fu, and J. I. A. Li, “Angle-resolved transport non-reciprocity and spontaneous symmetry breaking in twisted trilayer graphene,” *Nature Materials* **23**, 356–362 (2024).
- [41] Dmitry V Chichinadze, Naiyuan James Zhang, Jiang-Xiazi Lin, Xiaoyu Wang, Kenji Watanabe, Takashi Taniguchi, Oskar Vafek, and JIA Li, “Observation of giant nonlinear Hall conductivity in Bernal bilayer graphene,” arXiv preprint arXiv:2411.11156 (2024).

## METHODS

In this section, we provide additional discussion to further substantiate the results presented in the main text. We elaborate on the details of the transport measurements, examine the role of transport anisotropy within the relevant portion of the phase space, and summarize the characteristic transport signatures of the quantum Hall states observed within regime I.

### Angle-resolved transport measurement

In this work, the R6G sample is patterned into a sunflower geometry, enabling angle-resolved transport measurements. This approach is particularly advantageous given that the key phenomena under investigation emerge from a region of phase space characterized by extreme transport anisotropy.

Figure M1 shows an optical image of the sample, along with typical measurement configurations used throughout this study. The sunflower geometry, in combination with angle-resolved transport techniques, has been extensively employed in previous experimental works [24, 30, 40, 41]. As such, the detailed methodology will not be repeated here.

The angular transport response of the relevant phases has been thoroughly characterized. As shown in Fig. M2, the conductivity matrices corresponding to the stripe order, the metallic phase within regime I, and the quarter-metallic phase at high density are extracted from an extended set of angle-resolved measurements. In Figs. M2b–d, each point in the  $n$ - $D$  plane is probed using more than 30 independent configurations, providing sufficient constraints to fully determine the conductivity matrix. The resulting best fits, shown as solid black lines, show excellent agreement with the data and confirm accurate identification of the underlying anisotropy.

Crucially, this expansive dataset enables an unambiguous identification of a uniform sample, in which the transport response across many electrical contacts is governed by a single, well-defined conductivity matrix.

Figure M3a presents the  $n$ - $D$  map of transport anisotropy, defined as  $\xi = (R_{\max} - R_{\min}) / (R_{\max} + R_{\min})$ , measured at  $B_{\perp} = 0$ . The stripe regime exhibits extreme anisotropy, with  $\xi$  approaching unity, shown in red on the chosen color scale. In contrast, regimes I, II, and III display markedly reduced anisotropy.

The application of an out-of-plane magnetic field rapidly suppresses anisotropy within the stripe regime, as shown in Fig. M3b. Here, anisotropy is quantified by the ratio of conductivities along the two principal axes, extracted from extensive angle-resolved measurements similar to those in Fig. M2b–d. At  $B_{\perp} = 0.5$  T, this conductivity ratio is reduced by more than three orders of magnitude relative to its zero-field value. Thus,

the  $B$ -induced superconducting phase and its accompanying quantum Hall states do not exhibit strong transport anisotropy. Unless otherwise specified, measurements presented in the main text are performed along  $\phi = 90^{\circ}$ , using the configurations shown in Fig. M1b.

Unlike the stripe regime, where the orientation of the principal axis  $\alpha$  remains largely unaffected by the out-of-plane magnetic field  $B_{\perp}$ , regime I exhibits a pronounced rotation of  $\alpha$  with increasing  $B_{\perp}$ . As shown in Fig. M3c, the principal axis rotates by approximately  $15^{\circ}$  between  $B_{\perp} = 0$  and 1 T. This field-induced rotation may be closely related to the unusual stability of the superconducting phase, potentially reflecting a reconfiguration of the underlying momentum-space order.

### Characteristics of Quantum Hall States within Regime I

We summarize below the key features of the quantum Hall states observed within regime I, beginning with those that are consistent with conventional expectations for the quantum Hall effect:

*i.* The transport response exhibits vanishing longitudinal resistance and a finite Hall resistance at low temperature. As shown in Fig. 1g, the Hall resistance changes sign upon reversing the magnetic field direction. This behavior corresponds to a conductivity matrix with vanishing diagonal components and nonzero, antisymmetric off-diagonal components—characteristic of an incompressible quantum Hall state.

*ii.* Each quantum Hall state emerges along a trajectory with a well-defined Středa slope in the  $n$ - $B$  plane, indicating a fixed carrier density per flux quantum.

Next, we list the features that deviate from conventional expectations for the quantum Hall effect:

*i.* Quantum Hall states typically exhibit a gradual onset as a function of temperature, as shown in Fig. M6b. In particular, the Hall resistance in the center of a quantum Hall plateau remains largely temperature-independent, as its value is set by the underlying charge carrier density, which is unaffected by thermal fluctuations. In contrast, the quantum Hall states within regime I display sharp temperature-dependent onset in both  $R_{xx}$  and  $R_{xy}$ . As temperature increases above this onset, the Hall resistance  $R_{xy}$  decreases substantially. This behavior implies that the density of free charge carriers changes across the this transition or sharp crossover. Similarly,  $R_{xy}$  exhibits sharp changes as carrier density  $n$  is detuned from quantum Hall states, as shown in Fig. 2b and Fig. 3a–b.

*ii.* The stability of the quantum Hall effect is typically highly dependent on the out-of-plane magnetic field, which determines the robustness of incompressible signatures with increasing temperature. However, in regime I, the sharp temperature onset of transport signatures ap-

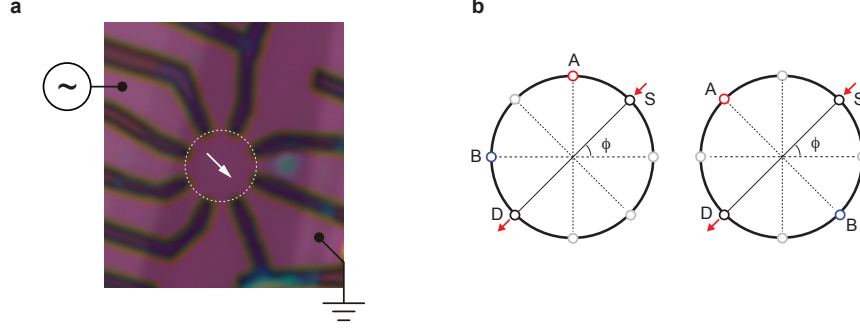


FIG. M1. **Sample geometry.** (a) Optical image of the R6G sample, patterned into the sunflower geometry: a disk-shaped channel with eight electrical contacts. (b) Schematic diagram of two measurement configurations. In the left (right) panel, voltage is measured between contacts aligned parallel (perpendicular) to the current flow direction. In the quantum Hall regime, these configurations yield measurements consistent with the longitudinal and transverse resistances,  $R_{xx}$  and  $R_{xy}$ . In angle-resolved transport measurements, the measurement angle  $\phi$  is operationally defined by the line connecting the two contacts used for current injection (source and drain).  $\phi = 0$  refers to the configuration where the left and right contacts in panel (a) serve as drain and source, respectively.

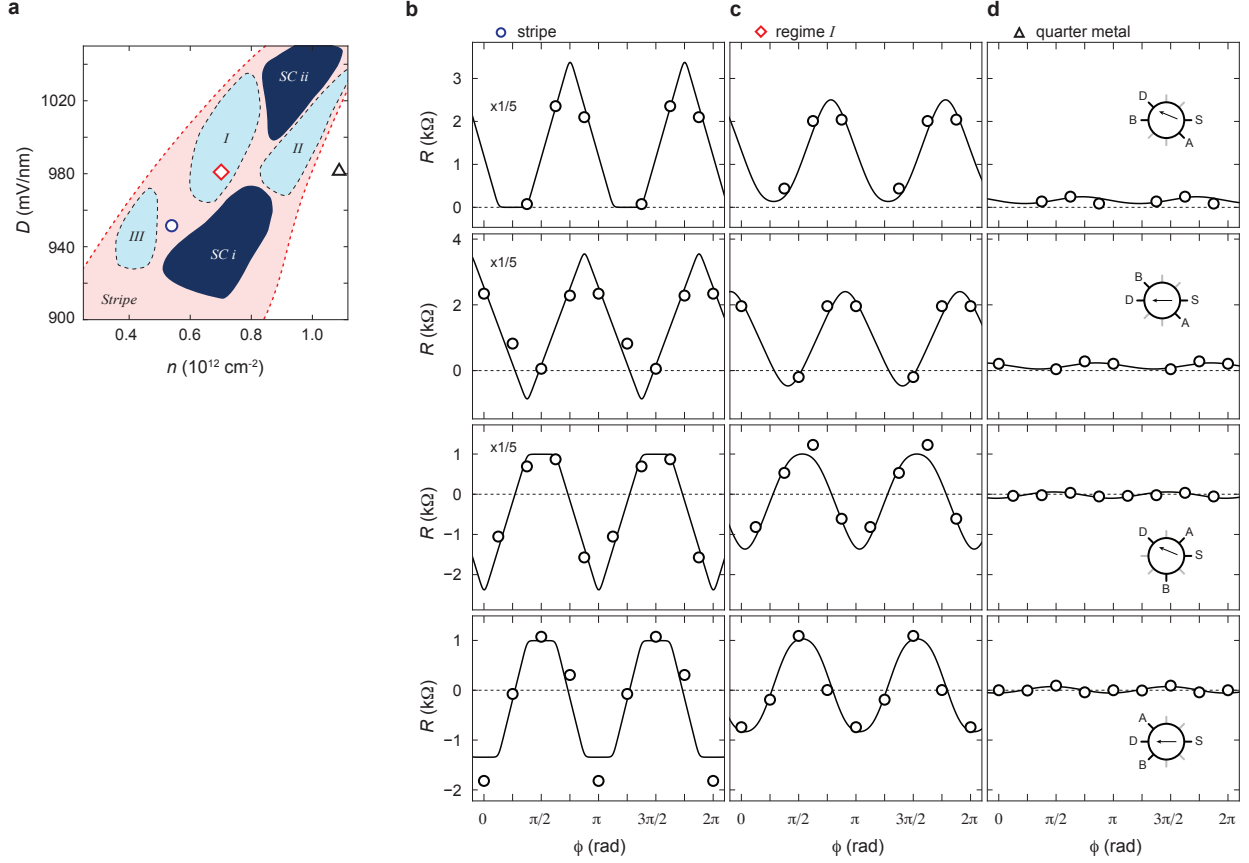


FIG. M2. **Angle-resolved transport and conductivity matrix.** (a) Schematic phase diagram around the stripe regime, showing regimes I, II, III, and the zero-field superconducting phases. (b–d) Angle-resolved measurements using an extended set of configurations: (b) inside the stripe regime, (c) inside regime I, and (d) in the quarter-metal phase on the high-density side of the stripe regime. Inset in panel (d) shows the measurement configuration used for each row. Solid black lines represent the best fits using a conductivity matrix model, yielding anisotropy ratios of  $\sigma_{\max}/\sigma_{\min} = 1000$  in the stripe regime,  $\sigma_{\max}/\sigma_{\min} = 4$  in regime I, and  $\sigma_{\max}/\sigma_{\min} = 1.5$  in the quarter-metal phase.

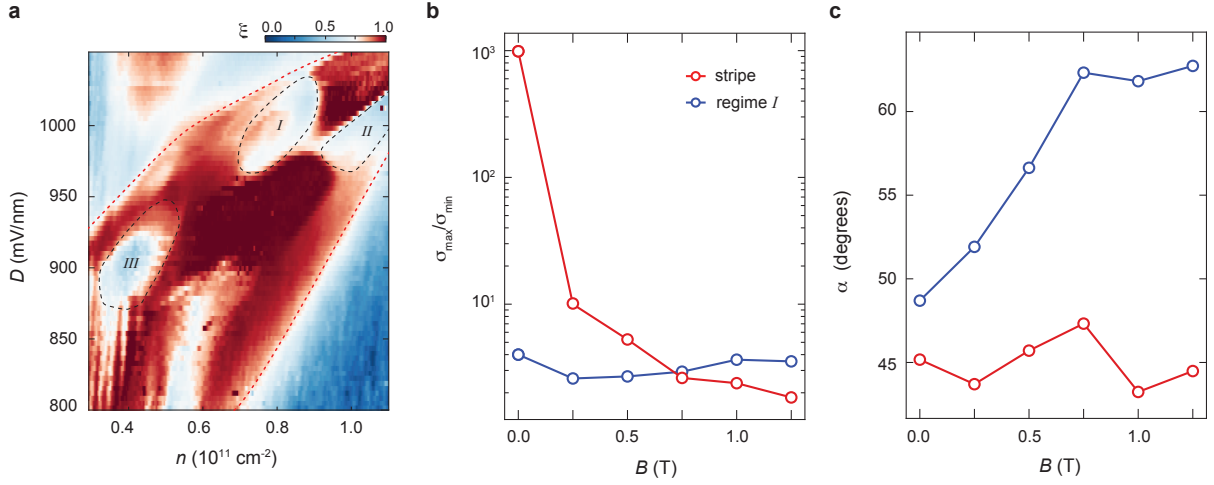


FIG. M3. **Evolution of anisotropy versus  $B_{\perp}$ .** (a) Transport anisotropy,  $\xi = (R_{\max} - R_{\min})/(R_{\max} + R_{\min})$ , measured across the  $n$ - $D$  regime of interest. (b) Intrinsic anisotropy, defined as the conductivity ratio  $\sigma_{\max}/\sigma_{\min}$ , and (c) principal axis orientation  $\alpha$ , both plotted as functions of  $B_{\perp}$ . Blue and red circles represent measurements from the stripe order and regime I, respectively. Values in (b-c) reflect the conductivity matrix, which is extracted from the full angle-resolved transport measurements shown in Fig. M2.

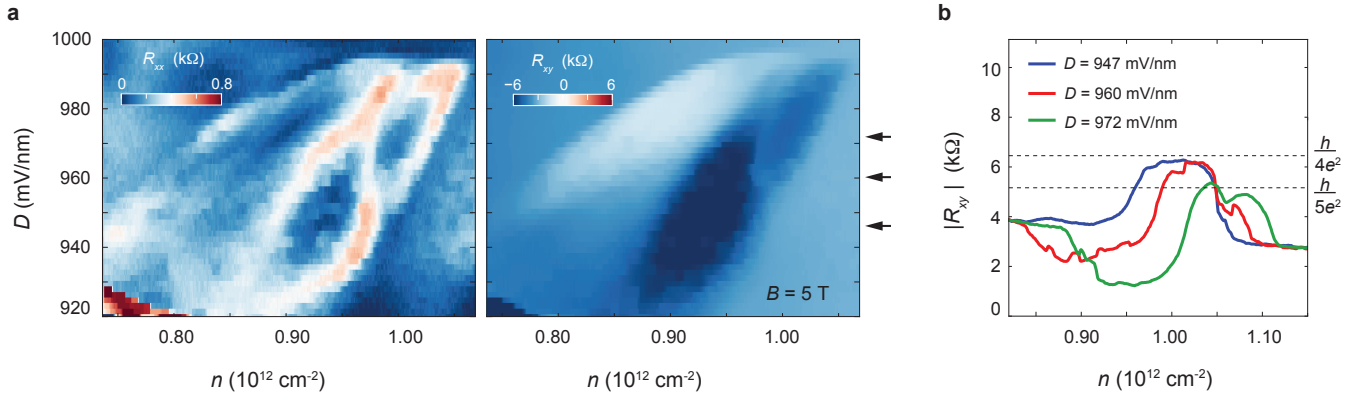


FIG. M4.  **$n$ - $D$  map across regime I.** (a)  $R_{xx}$  (left) and  $R_{xy}$  (right) as functions of  $n$  and  $D$  across regime I, measured at  $B_{\perp} = 5 \text{ T}$ . This  $n$ - $D$  map captures two quantum Hall states simultaneously. The boundary of each state is defined by a resistance peak in  $R_{xx}$ , while the two states exhibit distinct Hall plateau quantizations. (b)  $|R_{xy}|$  as a function of  $n$ , taken at constant  $B_{\perp}$  and  $D$  from the bottom panel of (a). Blue and red traces, measured at  $D = 947$  and  $960 \text{ mV/nm}$ , respectively, show Hall plateaus near  $h/4e^2$ . The green trace, taken at  $D = 972 \text{ mV/nm}$ , also exhibits a plateau near  $h/4e^2$ . Notably, the quantum Hall states do not track constant carrier density  $n$ ; instead, their positions in  $n$  shift systematically with  $D$ , as evident in Fig. 2 and panel (a). The map in panel (a) further reveals that the lower-density quantum Hall state disappears around  $D \approx 970 \text{ mV/nm}$ , seemingly replaced by the superconducting phase in the large- $D$  limit of regime I. This behavior suggests a possible competition between superconductivity and the quantum Hall states.

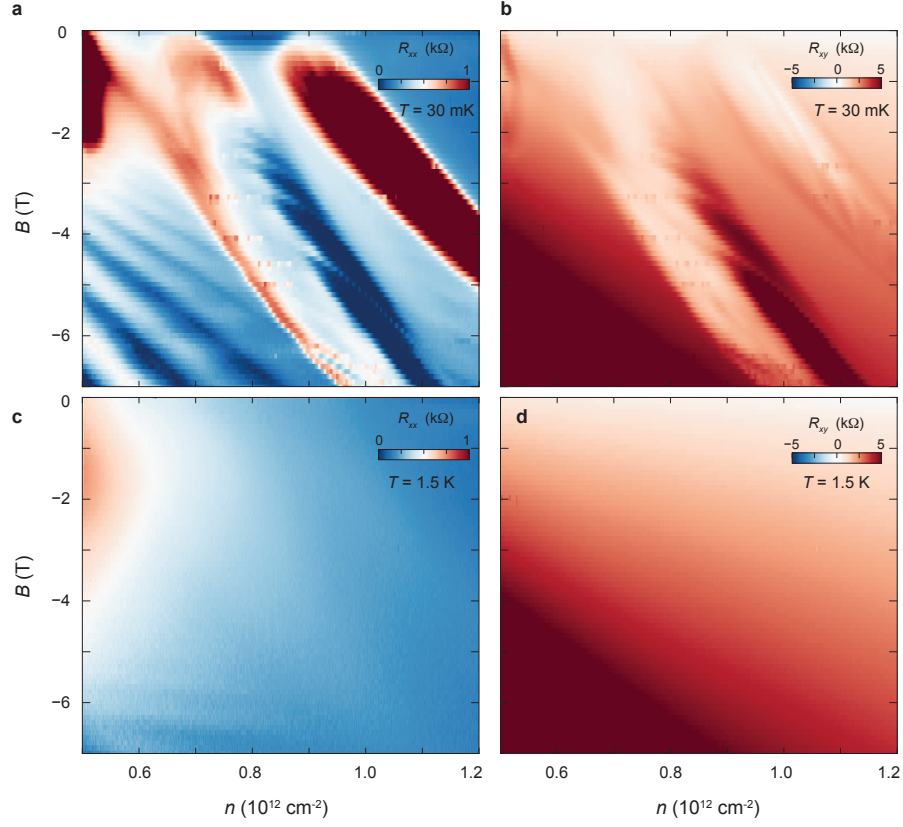


FIG. M5.  $n$ - $B$  plane at 1.5 K. (a-b)  $n$ - $B$  maps of (a)  $R_{xx}$  and (b)  $R_{xy}$  measured at  $T = 30$  mK. (c-d)  $n$ - $B$  maps of (c)  $R_{xx}$  and (d)  $R_{xy}$  measured at  $T = 1.5$  K. At  $T = 1.5$  K, the boundary of regime I, along with its associated superconducting and quantum Hall states, disappears.

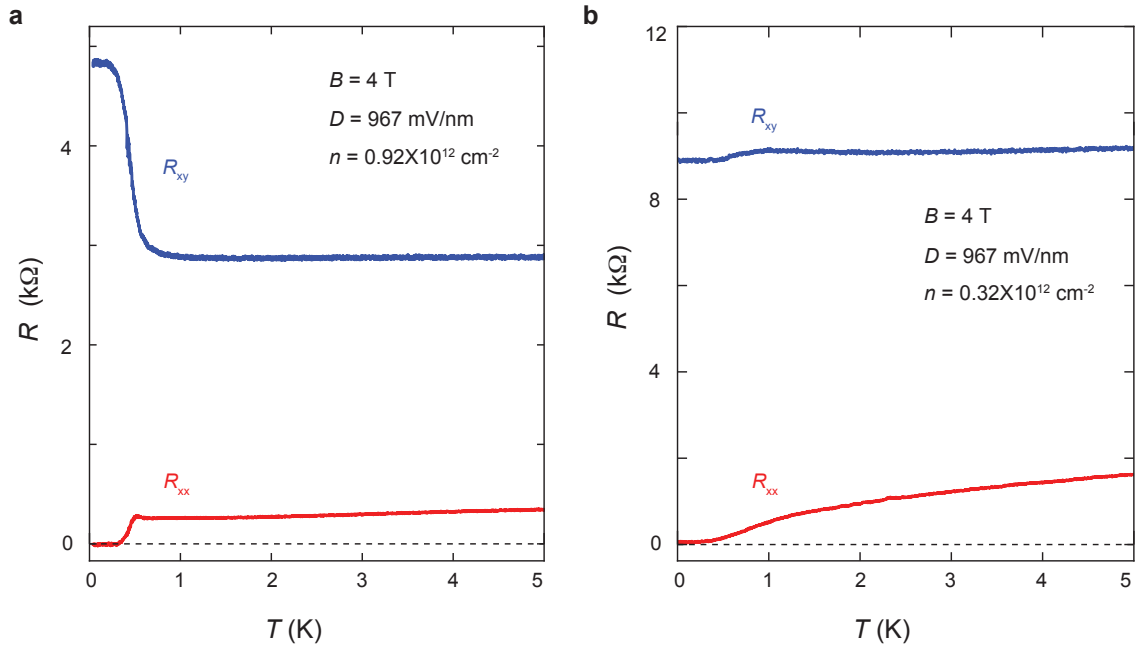


FIG. M6. **Transport signatures of quantum Hall effect.** Temperature dependence of longitudinal resistance  $R_{xx}$  (red traces) and Hall resistance  $R_{xy}$  (blue traces) measured at the same values of  $B$  and  $D$  fields: (a) inside regime I and (b) in an IQHE state emerging from the charge neutrality point. The comparison highlights the distinct onset behavior of the QHE states within regime I.

pears largely independent of magnetic field over a broad range of  $B_{\perp}$  (Fig. 3c). This insensitivity suggests that the quantum Hall effect in this regime relies on a parent order, such as a CDW phase with an onset temperature of approximately 0.5 K.

*iii.* Quantum Hall states in regime I emerge along both integer and half-integer Landau level fillings. Unlike in the conventional quantum Hall effect, where the Hall plateau value matches the Streda slope, the states in regime I display integer-quantized Hall plateaus that do not correspond to their Streda slopes.

### Regimes I, II, and III

As shown in Fig. M8a–b, the boundaries of regimes I, II, and III are sharply defined in the presence of an out-of-plane magnetic field. In the  $n$ - $D$  map measured at  $B_{\perp} = 3$  T, regimes II and III are delineated by prominent resistive peaks in  $R_{xx}$ .

On the high- and low-density sides of the stripe regime—corresponding to the upper left and lower right corners of the  $n$ - $D$  map, respectively— $n$ -dependent SdH oscillations are clearly observed in  $R_{xx}$ . These oscillations provide insights into the degeneracy of the underlying Fermi surfaces. On the high-density side, the SdH oscillations are consistent with a Fermi sea possessing no internal degeneracy. Angle-resolved transport measurements further reveal minimal anisotropy in this regime.

Together with the observation of an anomalous Hall effect, these findings suggest that this region is occupied by a quarter-metal phase [20].

On the low-density side, the SdH oscillations indicate the presence of a larger electron-like surface coexisting with a smaller hole-like surface. The absence of an anomalous Hall effect suggests that this region is occupied by a half-metal phase, in which an electron Fermi sea and a hole Fermi sea reside in opposite valleys.

The region of phase space between regimes I and II corresponds to the stripe-ordered phase at  $B_{\perp} = 0$ . Notably, SdH oscillations are absent within this intermediate regime, presenting an experimental challenge for identifying the underlying electronic order. However, the presence of an anomalous Hall effect—observed in both regime I and II, as shown in Fig. M10—suggests that the system is at least partially valley polarized, if not fully polarized.

In the  $n$ - $-B$  planes, regimes II and III exhibit behavior analogous to regime I. Figure M8c presents measurements of  $R_{xx}$  across an  $n$ - $B$  slice at fixed displacement field  $D = 935$  mV/nm. Here, regime III manifests as a pronounced resistive feature, bounded by lines with a Streda slope of  $t = 2$  (black dashed lines).

In contrast, regime II exhibits a boundary with a Streda slope of  $t = 3.5$  in the  $n$ - $B$  plane.

The precise relationship between regimes I, II, and III remains an open question and may hint at a broader framework of topological structure that develops within the stripe regime.

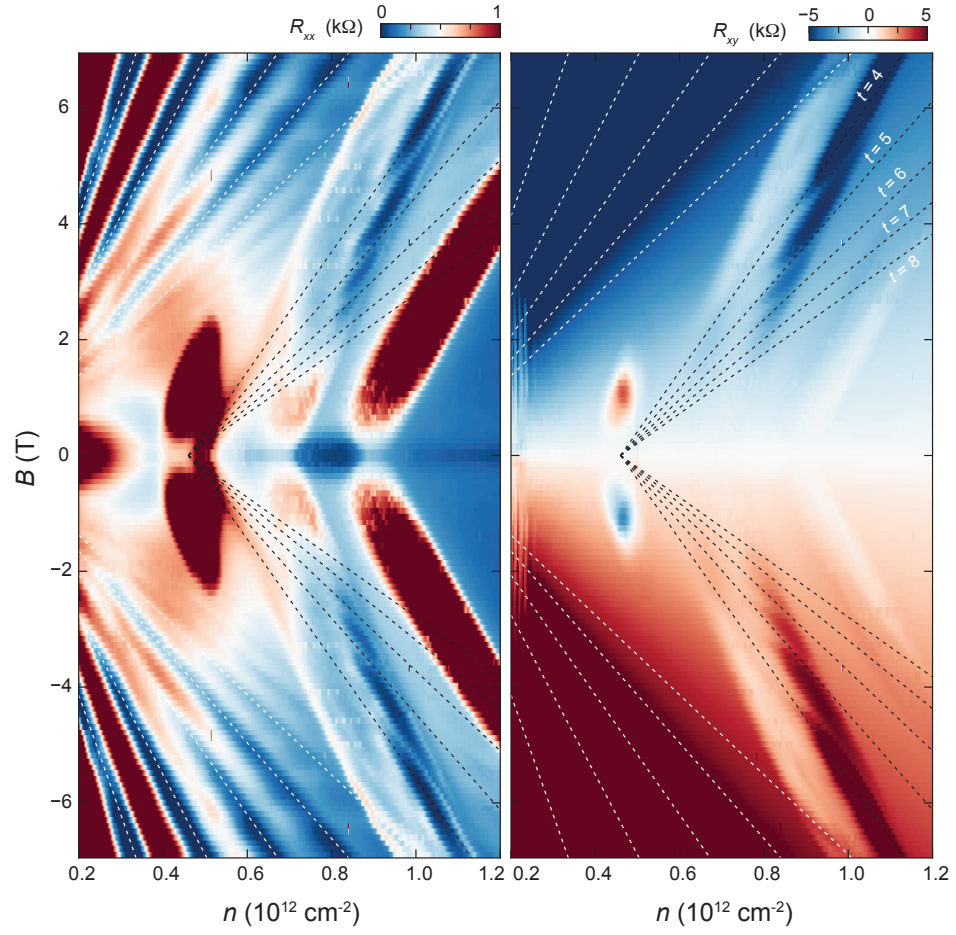


FIG. M7. **Fitting with integer Streda slopes.** Attempted fit of the quantum Hall states using a sequence of lines with integer Streda slopes. While the  $t = 4$  line is aligned with the center of one quantum Hall state, the remaining lines are clearly mismatched relative to the actual states.

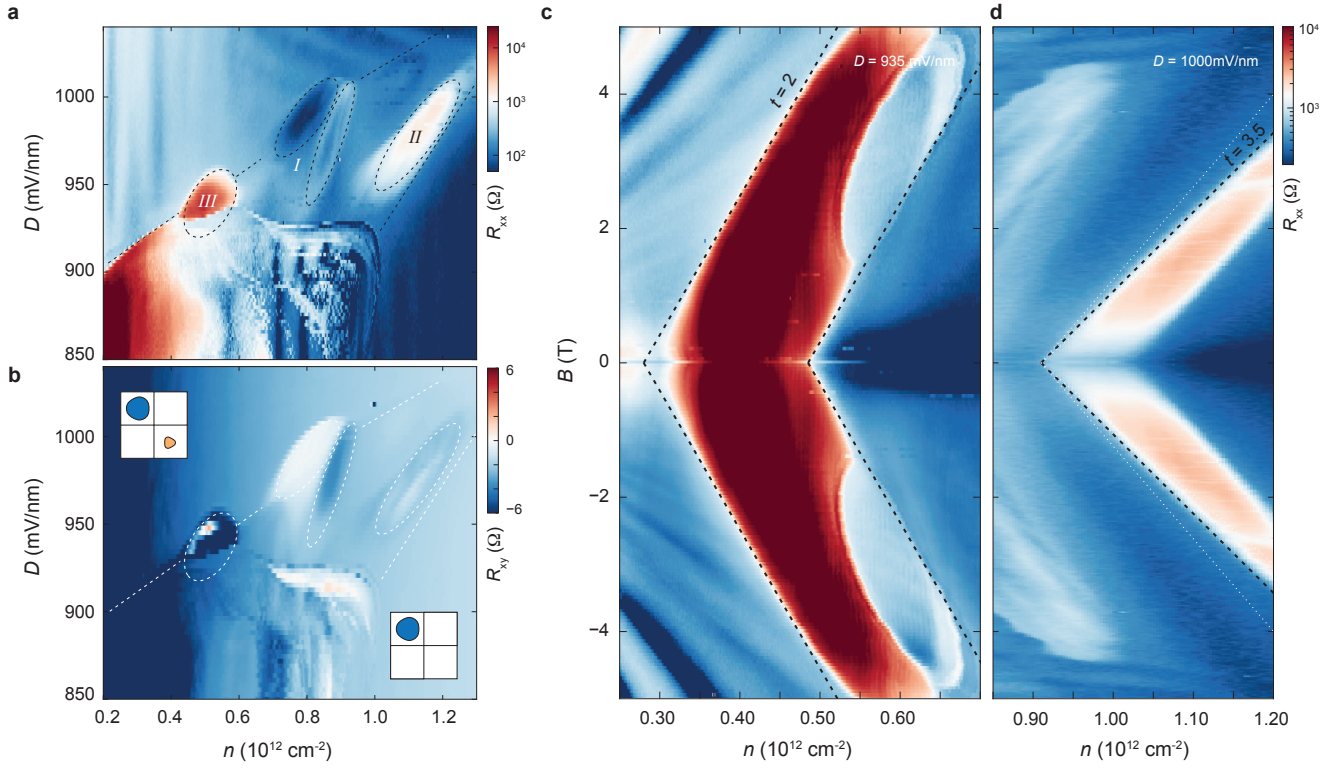


FIG. M8. **Regimes I, II, and III.** (a–b)  $n$ – $D$  maps of (a)  $R_{xx}$  and (b)  $R_{xy}$  measured at  $B = 3$  T. The superconducting and quantum Hall states in regime I are indicated with separate dashed circles. (c–d) Longitudinal resistance  $R_{xx}$  plotted across the  $n$ – $B$  plane, highlighting the evolution of regime (c) III and (d) II. In panel (d), the black dashed line marks the Streda slope  $t = 3.5$ , while the white dotted lines mark the integer slopes  $t = 3$  and  $t = 4$ . The boundary of regime II, highlighted by the black dashed line, clearly deviates from the lines with integer slopes.

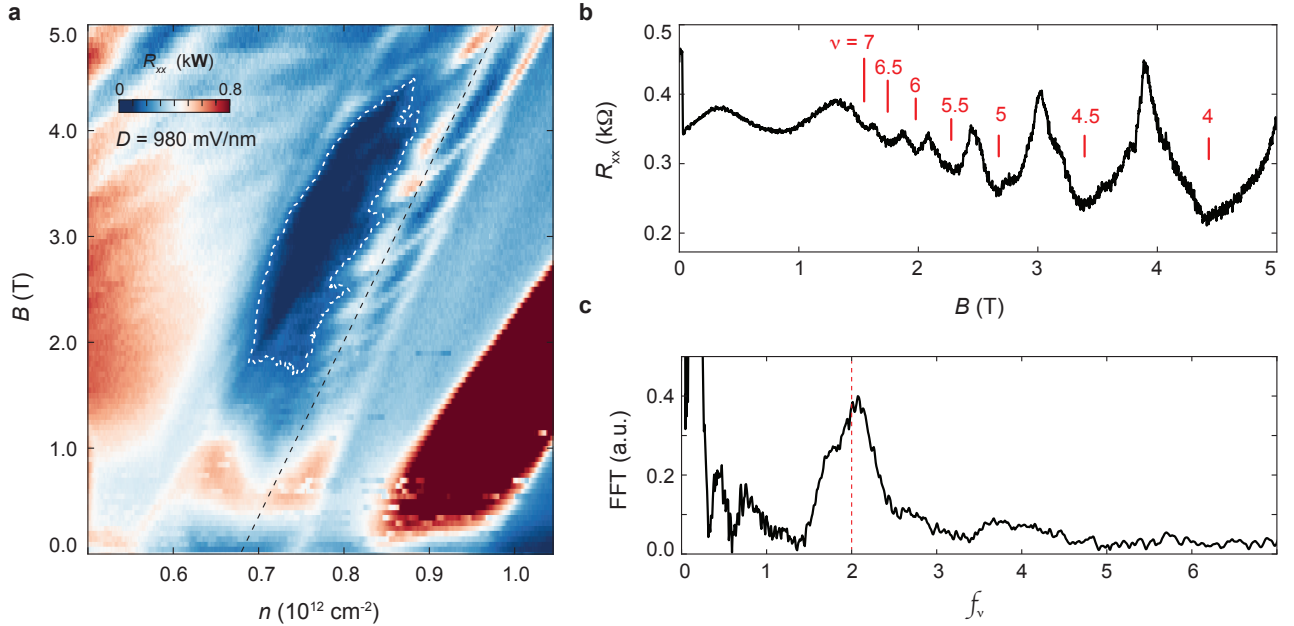


FIG. M9. **Shubnikov–de Haas oscillations across the quantum Hall sequence in regime I.** (a)  $R_{xx}$  as a function of  $n$  and  $B$  across regime I at  $D = 980$  mV/nm. (b) Shubnikov–de Haas (SdH) oscillations measured along the black dashed line in panel (a). (c) Fast Fourier transform (FFT) of the oscillations, showing a prominent peak at  $f_\nu = 2$ .

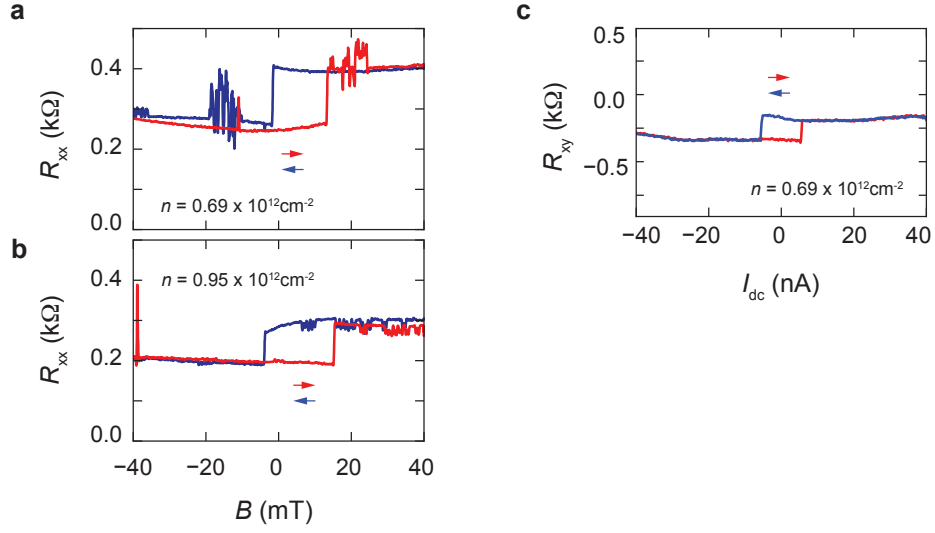


FIG. M10. **Hysteresis and anomalous Hall effect.** (a–b) Hysteresis loops in  $B_{\perp}$ -sweeps measured inside (a) regime I and (b) regime II, indicating the presence of an anomalous Hall effect. (c) In regime II at  $B_{\perp} = 0$ , hysteretic transitions in transport response can also be induced by sweeping the d.c. current bias back and forth. Together, these observations are consistent with orbital ferromagnetism in regimes I and II.